

(12)

(19)

(11)

2 163 252 A

(43) Application published 19 Feb 1986

(22) Date of filing **23 Jul 1985**

**(30) Priority data**

**(31) 8420760**

**(32) 15 Aug 1984**

**(33) GB**

**(71) Applicant**

**United Kingdom Atomic Energy Authority (United Kingdom),  
11 Charles II Street, London SW1Y 4QP**

**(72) Inventor**

**Thomas Andrew Lennox**

**(74) Agent and/or Address for Service**

**A R Collingwood,**

**Patents Branch, United Kingdom Atomic Energy  
Authority, 11 Charles II Street, London SW1Y 4QP**

(51) INT CL<sup>4</sup>

**G01T 1/22**

**(52) Domestic classification**

**G1A A12 A1 A4 C10 C12 D10 D12 D6 G10 G14 G17  
G7 HP P10 P5 R1 R2 R7 RQ RX S6**

U1S 1906 1968 2158 2159 2167 2172 2190 2312  
2314 2316 G1A

**(56) Documents cited**

**GB 1253639**

**GB 0949826**

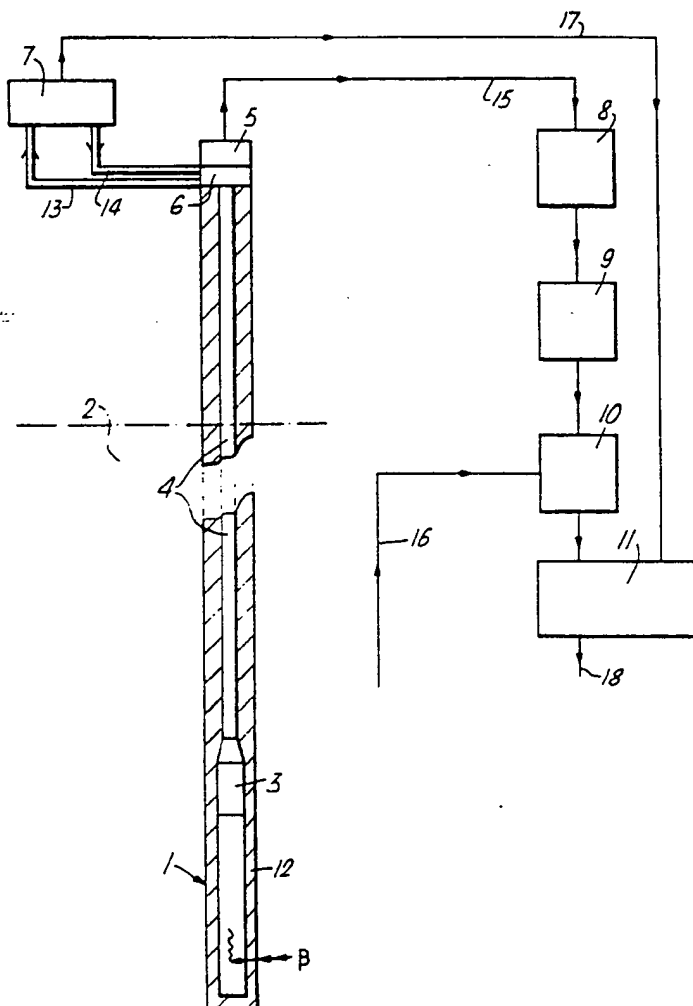
**(58) Field of search**

**G1A**

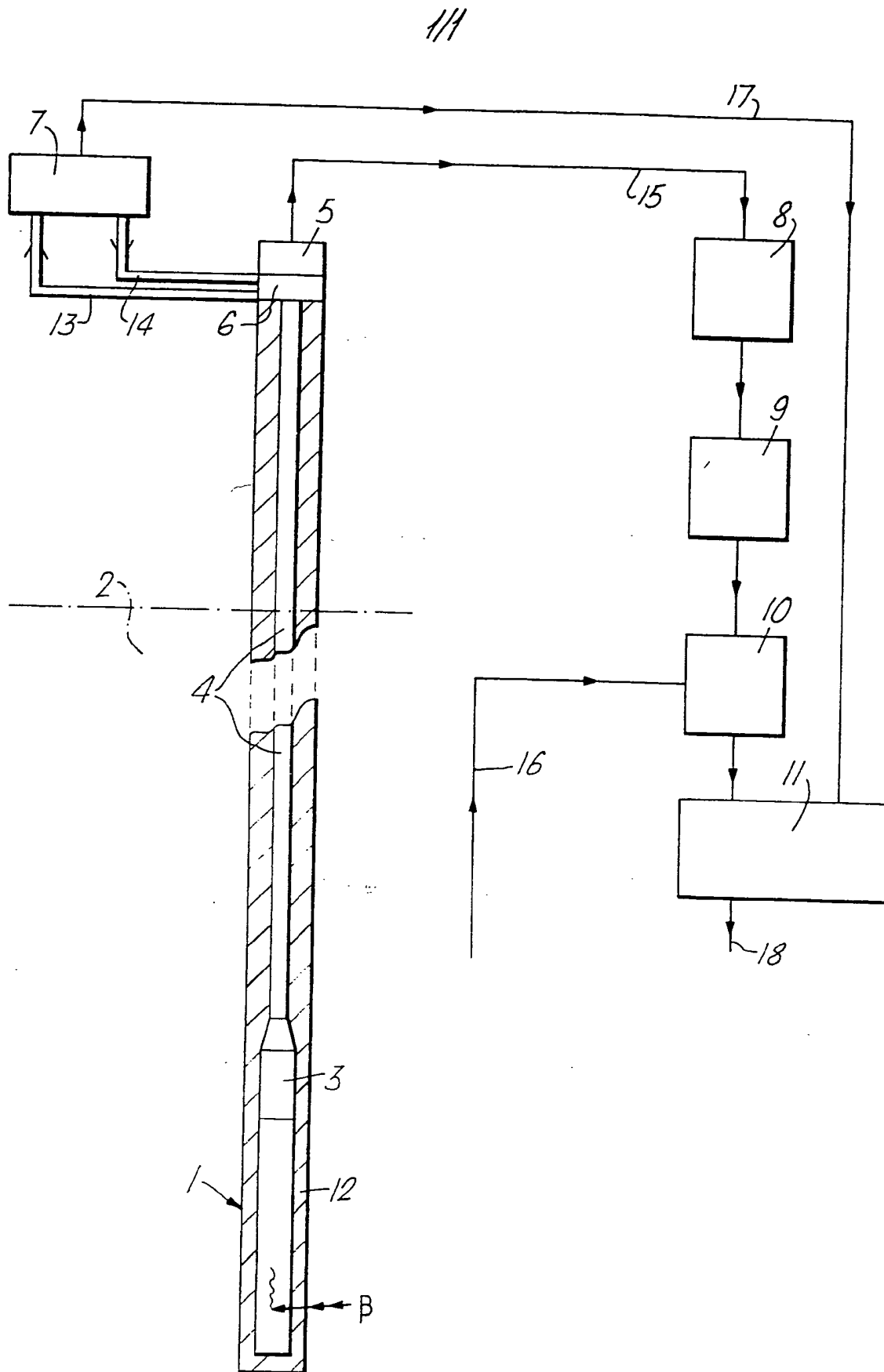
**(54) Monitoring of activity in**

(57) A detector is used to monitor the fluid coolant pool 2 of a nuclear reactor and operates by detecting short-lived fission or activation products by the Cerenkov radiation they produce.

The detector includes a Cerenkov detector head 1 connected by an optical fibre bundle 4 extending through pool 2 to a photosensitive detector 5. The output signal from detector 5 is passed to a comparison unit 10 and processing unit 11 for examination, evaluation and presentation of output signal data for suitable use e.g. detection of failed fuel or changes in density of the pool. An optical test unit 7 monitors the photosensitive detector 5.



002103232A



## SPECIFICATION

**Improvements in the monitoring of activity in remote environments**

- 5 This invention relates to the monitoring of activity in remote environments, and in particular to the monitoring of Beta particle activity.
- 10 It has been known for some time that when a Beta particle—an electron—traverses a transparent medium, light, called Cerenkov radiation, after the discoverer of the phenomenon, is emitted provided the velocity of the
- 15 particle is greater than the speed of light in the medium. Thus the amount of the Cerenkov radiation is related to the energy of the Beta particle (electron).
- It has been proposed to detect the leakage
- 20 of fission products into a reactor water-cooling system by detecting the high energy electrons from a few selected isotopes using a counter which relies on the Cerenkov effect. The counter is constituted by a photomultiplier tube
- 25 viewing the water. The pulses produced by the photomultiplier tube are proportional to the Cerenkov radiation emitted, and a discriminator is set to pass only pulses produced by electrons with energy 5MeV or greater. This
- 30 effectively separates the high energy electrons from both low energy electrons and photomultiplier tube noise. A choice of fission products which emit high energy Beta Particles includes  $\text{Br}^{87}$  (half life 55.6 sec, Beta energy
- 35 8.0MeV),  $\text{I}^{136}$  (86.0 sec, 6.4MeV),  $\text{Rb}^{90}$  (2.7 min, 5.7MeV),  $\text{Y}^{94}$  (16.5 min, 5.4MeV), and  $\text{Kr}^{88} \rightarrow \text{Rb}^{88}$  (2.77 hrs, 5.3MeV). The employment of the latter is particularly advantageous for small fuel element can ruptures, since the
- 40 long half-life allows ample time for the fission products to diffuse into the water without being seriously depleted by decay.

- According to the invention, a detector for monitoring the fluid coolant of a nuclear reactor operates on the detection of short-lived fission or activation products by the Cerenkov radiation they produce, and comprises a Cerenkov radiation detector head disposed in the fluid coolant, optical coupling means for
- 50 transmitting the radiation to a photosensitive detector outside the fluid coolant environment, and circuitry for receiving the output from the photosensitive detector for signal evaluation at a data receiving position.
- 55 The optical coupling means may be an optical fibre bundle which enables non-linear connection between Cerenkov and photosensitive detectors. The detection applications envisaged may include a failed fuel monitor by
- 60 detection of short-lived (eg. half-lives from 1/10th second to 150 seconds) fission products in the bulk coolant by a detector situated at a position in the bulk coolant such as to minimise the effects of radiation, to be
- 65 employed in conjunction with more localised

- 70 detectors, which can be of the same kind or of another kind such as delayed neutron detectors, situated at the fluid coolant outlets from individual fuel element sub-assemblies, such detection may be concerned with the
- 75 fuel of gas-, water-, or liquid metal-cooled nuclear reactors. Other applications include monitoring of the oxygen level in the sodium pool of a fast reactor by detection of the Beta emission from the activation product  $\text{N}^{16}$ , reactor power measurement by monitoring the Beta emission arising from the Compton scattering of prompt gamma rays from the fission process in the fuel, decay heat measurement
- 80 by monitoring the Beta emission from the Compton scattering of gamma ray flux from fission product decay, and monitoring for changes in the density of the sodium in the pool of a fast reactor by monitoring changes
- 85 in the Beta emission from changes in gamma ray attenuation of the sodium.
- Also relevant are the monitoring of Beta rays from the short-lived isotopes  $\text{F}^{20}$  and  $\text{Ne}^{23}$ . The maximum energy of these isotopes
- 90 (5.4MeV and 4.4MeV respectively) is much greater than that for  $\text{Na}^{24}$  (1.39MeV) and thus a detector could be used for detecting in-core for variation in the  $\text{F}^{20}$  and  $\text{Ne}^{23}$  concentration and hence variation in flow in the subassemblies—eg. due to blockage build-up.
- 95 A typical detector of the above kind, together with its associated circuitry will now be described by way of example with reference to the sole Figure of the accompanying drawing
- 100 which is a diagrammatic side view partly in section.
- The detector includes a Cerenkov detector head 1 disposed in the sodium pool 2 of a fast reactor and including elongate shield or
- 105 containment 12. Beta particles radiating in the pool give rise to Cerenkov radiation which is focused by a focusing system 3 into a beam which is transmitted by an optical fibre bundle 4 extending through and out of the pool 2 to
- 110 a photosensitive detector head 5 with interposition of an optical coupler 6 for a test pulse which can be generated for testing the equipment and employed with an optical performance test unit 7 via lines 13, 14. The output
- 115 signal from the photo-sensitive detector head 5 is transmitted on line 15 to an amplifier 8, from thence to a discriminator 9 which is set to a range of pulse heights which it is desired to monitor (for example, for prompt gamma
- 120 rays less than 5MeV, for fission products 5–8MeV, and for  $\text{N}^{16}$  decay greater than 8MeV), from thence to a signal comparison unit 10 into which is also fed on line 16
- 125 signals from other detectors of the same type when multihead monitoring is to be effected. A signal processing unit 11 is employed for the examination, evaluation and presentation of signal data in the context of the particular application for which the detector is intended,
- 130 some of which are set forth earlier. There is

also an input to the signal processing unit 11 on line 17 in the form of an optical performance signal from the test unit 7 for test and possibly also calibration purposes. It is envisaged that this would be helpful for indication of any deterioration of performance due to radiation damage. The output signal on line 18 from unit 11 may be used to provide a running visual monitor indication or may have other or additional uses, for example to provide failed fuel detection, or other control or data presentation apparatus.

It is possible with combination of signals from other detectors of the same type to eliminate background signals by subtraction. One detector can be isolated from the Beta activity in the sodium pool and employed to monitor prompt gamma flux after Compton scattering.

Advantages include simplicity of construction and ease of replacement, elimination of routing any electrical cables into the pool environment, and very small detector resolving times with very high count rates. Furthermore the detector head can be coated with various shielding materials to give differential attenuation of Beta particles of various energies and hence optimisation of the detection of a particular source.

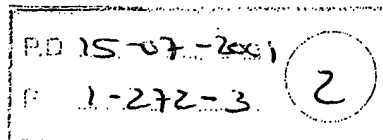
#### CLAIMS

1. A detector for monitoring the fluid coolant of a nuclear reactor comprising a Cerenkov radiation detector head disposed in the fluid coolant, optical coupling means for transmitting the radiation to a photosensitive detector outside the fluid coolant environment, and circuitry for receiving the output from the photosensitive detector for signal evaluation at a data receiving position.

2. A detector as claimed in Claim 1, in which the optical coupling means comprises an optical fibre bundle which establishes non-linear connection between Cerenkov and photosensitive detectors.

3. A detector as claimed in Claim 2, including an optical test unit associated with the photosensitive detector.

4. A detector for monitoring the fluid coolant of a nuclear reactor substantially as hereinbefore described with reference to and as shown in the accompanying drawings.



TuA3-1 (Invited)

## Smith-Purcell Radiation from Metallic and Dielectric Photonic Crystals

Kazuo Ohtaka

Center for Frontier Science, Chiba University, 1-33 Yayoi, Inage-ku,  
Chiba-shi, 263-8522 Japan  
Tel: +81-43-290-3500, Fax: +81-43-290-3512,  
E-mail: ohtaka@cfs.chiba-u.ac.jp

Smith-Purcell (SP) radiation from a charge running near a periodically grooved solid-state surface has a long history of investigation since the pioneering work of Smith and Purcell [1]. It is a kind of Cerenkov radiation, in which an evanescent photon emitted by the running charge turns to an observable one by the umklapp scattering by the periodic array of grooves; an evanescent photon originally present in the phase space outside the light line gets into the light cone when an umklapp shift of its momentum component takes place.

This paper treats a theoretical study of the SP spectrum from a photonic crystal, which is used in place of a grating as a source of the umklapp light scattering. We use as a model photonic crystal a periodic array of dielectric and metallic spheres, since the system of arrayed spheres is treated most compactly and strictly of all in solving Maxwell's equations [2][3]. The result of the calculation is expected to be applicable to any photonic crystal, including those obtained by, say, lithographic technique, with some changes added, appropriate to the system concerned but only quantitative in nature. Our calculation is composed of two steps, the first of obtaining the amplitude of the evanescent light emitted by a charge running parallel to the surface of the photonic crystal and the second of treating exactly the subsequent light scattering by it. The SP spectrum from an one-dimensional array of spheres is treated already by Garcia de Abajo [4]. Our concern lies in the full three-dimensional photonic crystals. In a previous paper [5], we demonstrated that the band structure of a photonic crystal was faithfully reproduced in its SP spectrum. The dependence of the intensity on the thickness of the slab photonic crystal was also examined; the overall intensity increases with thickness in a thin system, while in a system thick enough, having roughly more than several stacking layers, it saturates except at the positions of the resonance peaks. The heights of the peaks generally continue to grow up due to the enhancement of the Q values of the resonating photonic bands. The saturation comes from the evanescent nature of the initial light; the incident light sees only a few top layers, however thick the slab may be.

In this paper we are interested in (a) the difference of the SP spectrum between dielectric and metallic photonic crystals, (b) the effect of the umklapp scattering in the direction normal to the trajectory of charge and (c) the dependence of the spectrum with the charge velocity.

In the topic (a), it is shown that metallic photonic crystals give rise to the SP spectra order of magnitudes stronger than those of the dielectric case. We shall analyze this feature by using the Drude form of the dielectric constant for the metal spheres and calculate the band structure taking into account the plasmon resonances [6]. It is shown that the enhanced



# Cerenkov Radiation in Photonic Crystals

Chiyan Luo, Mihai Ibanescu, Steven G. Johnson,  
J. D. Joannopoulos\*

In a conventional material, the coherent Cerenkov radiation due to a moving charged particle is associated with a velocity threshold, a forward-pointing radiation cone, and a forward direction of emission. We describe different behavior for the Cerenkov radiation in a photonic crystal. In particular, this radiation is intrinsically coupled with transition radiation and is observable without any threshold. Within one particle-velocity range, we found a radiation pattern with a backward-pointing radiation cone. In another velocity range, backward-propagating Cerenkov radiation can be expected. Potential applications include velocity-sensitive particle detection and radiation generation at selectable frequencies.

When a charged particle travels inside a medium, it can drive the medium to emit coherent electromagnetic energy called Cerenkov radiation (CR) (1). Extensively used in particle detectors and counters (2), CR in a conventional material possesses three key characteristics: it occurs only when the particle's velocity exceeds the medium's phase velocity, the energy propagates only in the forward direction, and there is a forward-pointing conical wavefront. These characteristics remain qualitatively unchanged even in the presence of material dispersion (3–6). One possible source of unusual CR is in a medium with simultaneously negative permittivity and permeability, commonly known as a negative-index material for its reversal of Snell's law of refraction (7–12), in which CR is predicted to flow backward; i.e., opposite to the particle velocity (7). Another possibility exists near a periodic structure, where simple Bragg scattering of light can give rise to radiation without any velocity threshold. This was first confirmed by Smith and Purcell (13) in early experiments with electrons traveling near the surface of a metallic grating. CR has since been studied in one-dimensionally periodic multilayer stacks (14, 15), and the Smith-Purcell effect has been extended to near the surface of dielectric structures (16, 17). A photonic crystal (18–20), where very complex Bragg scattering is possible, presents a rich new medium for unusual photon phenomena (21–23). We reveal a variety of CR patterns that can occur in a single photonic crystal under different particle-velocity regimes.

CR in a photonic crystal arises from a coherent excitation of its eigenmodes by the moving charge. Its origin lies in both the transition radiation, which occurs when the

charge crosses a dielectric boundary or experiences an inhomogeneous dielectric environment, and the conventional CR, in which coherence is preserved throughout the medium. Both effects are incorporated in our approach. However, unlike the Smith-Purcell effect, in which radiation is generated via a periodic grating but then propagates through a uniform medium, this CR is generated and propagates within the same crystal in the form of Bloch waves. The properties of these Bloch waves can be substantially different from waves in a uniform medium, leading to effects not previously anticipated. In one case, we can reverse the overall cone that encloses all traveling electromagnetic energy. In another situation, we demonstrate a backward-propagating CR behavior reminiscent of that predicted in negative-index materials. These are very general results based on direct solutions of Maxwell's equations and should find applications in particle detection and wave production techniques.

For simplicity, we focus on a two-dimensional photonic crystal (Fig. 1). Let a charge  $q$  move in the (01) direction of a square lattice of air holes in a dielectric, in the  $xz$  plane, with parameters as specified in the Fig. 1 legend. Figure 1A shows the calculated transverse electric (the electric field in the  $xz$  plane, appropriate for CR) band structure of this photonic crystal. We take the particle's motion to be in the  $z$  direction and consider a path where the particle does not cross dielectric interfaces (Fig. 1B, inset). As a reference, the long-wavelength phase velocity ( $v_c$ ) of this photonic crystal is  $v_c = 0.44c$  (where  $c$  is the speed of light). The excited radiation can be determined by treating the charge as a source with space-time dependence  $\delta(\mathbf{r}-\mathbf{v}t) = \sum_{\mathbf{k}} e^{i\mathbf{k} \cdot \mathbf{r} - i\mathbf{k} \cdot \mathbf{v}t}$ , that is, as a superposition of planewaves with different wave vectors  $\mathbf{k}$  and frequencies  $\mathbf{k} \cdot \mathbf{v}$ , where  $\delta$  is the Dirac delta function,  $e$  is the base of the natural logarithm,  $i$  is the unit of imaginary numbers,  $\mathbf{r}$  is

the position, and  $t$  is the time. Bloch waves arise from the resonance of a planewave source with the photon dispersion relation

$$\omega_n(\mathbf{k}) = \mathbf{k} \cdot \mathbf{v} \quad (1)$$

where  $\omega$  is the frequency,  $n$  is the band index, the wave vector  $\mathbf{k}$  can include an arbitrary reciprocal lattice vector  $\mathbf{G}$ , and  $\omega_n(\mathbf{k}) = \omega_n(\mathbf{k} + \mathbf{G})$ . The CR consists of modes satisfying Eq. 1 (24), which can be found in  $\mathbf{k}$

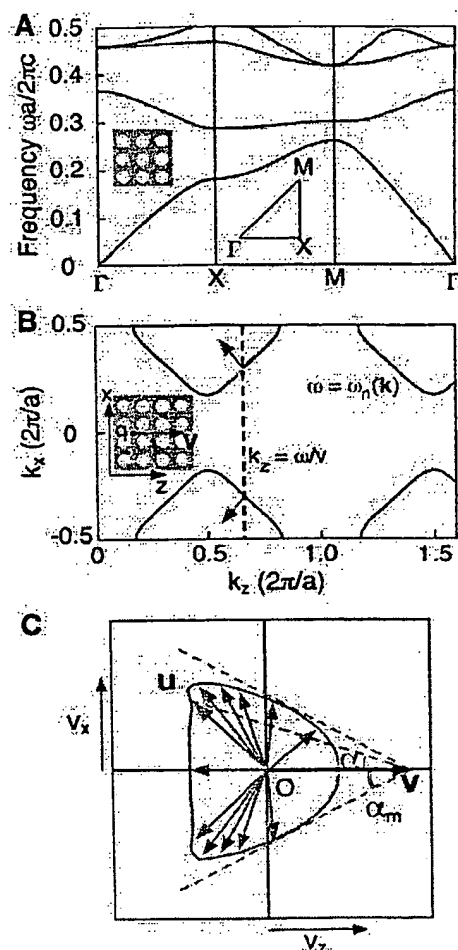


**Fig. 1.** Band structure and analysis of CR in a photonic crystal. (A) Transverse electric band structure of a two-dimensional square lattice of air columns in a dielectric (dielectric constant  $\epsilon = 12$ ) with column radii  $r = 0.4a$ ,  $a$  being the lattice period. The crystal structure and the irreducible Brillouin zone are shown as insets.  $\Gamma$ , X, and M are, respectively, the center, edge center, and corner of the first Brillouin zone. (B) Method of solving Eq. 1 in  $k$  space. CR occurs when the  $k_z = \omega/v$  plane (dashed line) intersects a photonic-crystal dispersion surface. Blue arrows indicate the group velocities of CR modes. (C) Method of obtaining CR cone shapes. The group velocities for all modes obtained in (B) form a contour.  $\alpha$  is the cone angle for the mode with group velocity  $u$ , and  $\alpha_m$  gives the angle for the overall radiation cone (gray dashed lines). The angular density of the arrows roughly reflects the CR angular distribution.

Department of Physics and Center for Materials Science and Engineering, Massachusetts Institute of Technology, Cambridge, MA 02139, USA.

\*To whom correspondence should be addressed. E-mail: joannop@mit.edu

space by intersecting the plane  $\omega = k \cdot v$  with the dispersion surface  $\omega = \omega_n(k)$  (Fig. 1B). The CR behavior in real space, however, must be obtained from the group velocity  $u = \partial\omega/\partial k$ ; that is, the gradient vector to a dispersion surface, which can be shown to be the energy transport vector for each mode (25). The emission angle is given by the direction of  $u$ . Moreover, the radiation pattern can be deduced from  $u$  via the group velocity contour (Fig. 1C). We plot both the charge velocity  $v$  and the group velocities  $u$  of all the CR modes in a velocity space (26). The magnitude of  $u$  is proportional to the distance traveled by the wavefront of the associated photon mode, and the magnitude of  $v$  is proportional to the distance traveled by the

charged particle in the same time. Thus, the radiation wavefront for each mode lies on a "group cone" (3, 6) with its apex on the moving particle and a half-apex angle  $\alpha$ , the angle between  $v - u$  and  $v$ . A superposition of all group cones gives the overall CR pattern, and the maximum angle  $\alpha_m$  of all such  $\alpha$ 's is the half-apex angle for the overall cone. Propagating Bloch modes can only exist on the rear side of this overall cone, whereas the radiation fields are evanescent on the forward side, and across the overall cone the radiated field amplitude experiences a drop. In the special case of a uniform material, only the  $G = 0$  modes are excited and our approach yields the characteristics of conventional CR. For an electron traveling near a grating surface, one employs the dispersion relations of air along with diffraction to obtain the Smith-Purcell radiation.

In the present photonic crystal, we solved Eq. 1 using photon bands calculated by planewave expansion (27). We focused on the solutions with the lowest frequencies; higher-order modes with larger  $G$  or in higher bands can be analyzed similarly. Figure 2 shows the results for the CR emission frequency  $\omega$ , wave vector  $k$ , and group velocity  $u$ . We see that for  $v < v_c$ , the radiation coalesces into Smith-Purcell resonances around  $\omega \approx G \cdot v$ . For larger  $v$ , the resonances merge together to form emission bands outside which CR is inhibited (Fig. 2A). As  $v$  increases,  $k$  and  $u$  within each emission band are strongly influenced by the photonic band structure. We can identify four regimes of the charge velocity (Fig. 2, B and C) with four qualitatively different CR behaviors in a photonic crystal:

1)  $v \leq \sim 0.1c$  corresponds to the Smith-Purcell regime, in which the CR arises primarily through constructive interference between consecutive unit cells and in the first emission band corresponds to the first resonance near  $k_z = 2\pi/a$ , where  $a$  is the lattice period. The group velocity contour is approximately circular, with radius  $v_c$ . Because  $v < v_c$ , the overall wavefront will be roughly circular and centered on the slowly moving particle.

2) The regime  $v \approx 0.15c$  is unique to the photonic crystal: The first and higher Smith-Purcell resonances merge into one band, in which the slow photon modes near the photonic band edge are in coexistence with the fast modes. As can be seen from the group velocity contours, in going from  $v = 0.1c$  to  $v = 0.15c$ , the modes in the forward direction begin to travel slower than the charged particle (and can even have negative group velocities), eventually producing a contour at  $v = 0.15c$  that winds around without enclosing  $v$ . Because in this band there are some fast modes in the forward direction whose  $u_z$  exceeds  $v$ , the radiation pattern here should

possess a backward-pointing overall cone ( $\alpha > \pi/2$ ), according to the analysis of Fig. 1C. This is therefore the reversed-cone regime. Such a reversed cone is forbidden by causality (1) in a uniform passive medium.

3) In the  $\sim 0.2c \leq v \leq \sim 0.4c$  regime, all the radiation modes in the lowest emission band reside in the region  $\pi/a < k_z < 2\pi/a$  with  $u_z < 0$ , which implies that the energy flows opposite to  $v$  in this band. The overall cone is now pointing forward and, as described below, the radiation becomes collimated in a backward direction. CR here is strongly similar to the predicted behavior in a negative-index material. However, because  $k' \cdot u > 0$  in this regime (where  $k'$  is the Bloch-reduced  $k$  in the first Brillouin zone), the photonic crystal may be regarded as an effective positive-index medium (22). We call this the backward-flux regime.

4) In the  $v \geq v_c$  regime, the solution to Eq. 1 starts from zero frequency, and the group-velocity contour becomes an open-ended curve with positive  $u_z$ . The charged particle now travels faster than all of the excited modes, and constructive interference is achieved throughout the whole photonic crystal. This behavior is identical to CR in a normal dispersive medium. Hence, this is the normal regime.

The CR showed less interesting transitional behavior for intermediate charge velocities between these regimes. For example, when  $\sim 0.4c < v < \sim v_c$ , the CR showed a mixture of forward and backward emissions similar to that depicted in Fig. 1C.

We confirmed our analysis by performing finite-difference time-domain (FDTD) simulations of radiation for a moving charge in this photonic crystal (28). We reproduce in Fig. 3A the velocity diagrams from Fig. 2C and present the resulting radiation-field simulations in Fig. 3B. To quantitatively demonstrate the backward radiation, we also plot in Fig. 3C the simulated flux through a fixed line perpendicular to  $v$  as a function of  $\omega$ . At the low velocity,  $v = 0.1c$ , the radiation shows a Smith-Purcell behavior of near-isotropic wavefront. As the velocity increases to  $v = 0.15c$ , the overall radiation cone indeed reversed as predicted. Further increasing of  $v$  to  $v = 0.3c$  steers the radiation to the backward direction, and if  $v$  is increased to  $v = 0.6c > v_c$  the familiar CR with a sharp forward-pointing cone as in a uniform medium is recovered. The angular distribution of radiation is directly visible (Fig. 3B). When  $v = 0.1c$  or  $0.15c$ , the radiation is distributed over a wide range of emission angles without producing a cone of intensity maxima. For  $v = 0.3c$  or  $0.6c$ , however, the CR becomes collimated, and a definite emission angle in both the forward and the backward direction for most of the radiation energy can be observed. In particular, the crystal-induced dis-

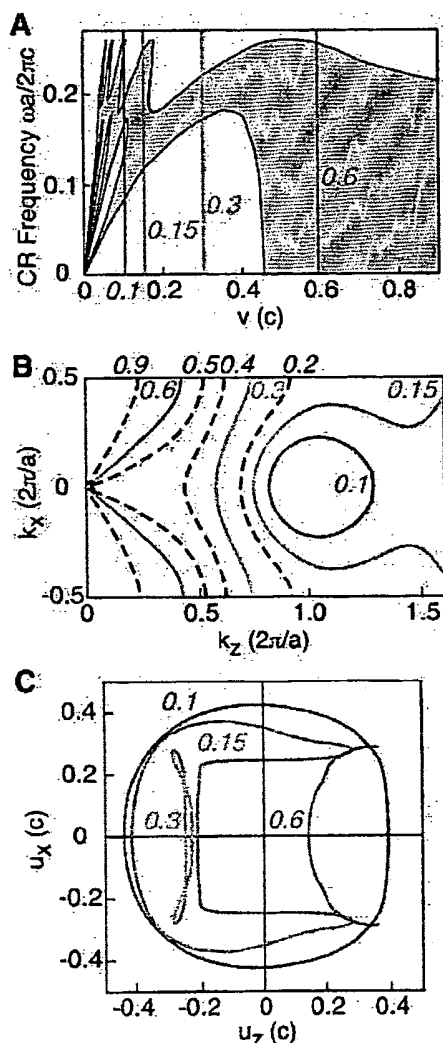


Fig. 2. Calculated CR modes with the lowest frequencies for the photonic crystal of Fig. 1. (A) The CR emission band structure (red region) in the first photonic band as a function of  $v$ . Colored vertical lines mark representative  $v$ 's for different CR behaviors. (B) The solution  $k$  for a few  $v$ 's indicated by the numbers in italics. (C) The group velocity contours for the representative values of  $v$ .



## REPORTS

person at  $v = 0.6c$  becomes so small that a strong intensity peak cone is formed and almost overlaps with the overall cone. A clear distinction between the CR behaviors for  $v < v_c$  and  $v > v_c$  is that for  $v > v_c$  the measured flux in the  $z$  direction is positive over the emission band, but for  $v < v_c$  certain frequency regions appear where the flux can be negative (Fig. 3C). Because positive and negative flux values can occur at the same frequency [e.g., at  $(\omega a)/(2\pi c) = 0.2$ ], this photonic crystal does not behave as a uniform negative-index medium, as noted before. Another distinction lies in the field pattern and is similar to that reported in (5) at a phonon resonance frequency: The near-static, nonradiating field extends beyond the overall cone when  $v < v_c$ , whereas for  $v > v_c$ , the field outside the cone is strictly zero. These near-static fields create an artificial peak around  $\omega = 0$  in Fig. 3C for  $v < v_c$  (as in  $v = 0.1c$ ) which we have verified to reduce to 0 for  $\omega \neq 0$  with increasing computational cell sizes and time steps. Finally, there are high-frequency radiation "tails," corresponding to higher-order radiation, behind the charge in all cases of Fig. 3B. The higher order modes typically have smaller group velocities and thus form dense forward-pointing cones of smaller angles, as first predicted in (6) (for coherently driven slow-light media). Here

these tails can exhibit a backward radiation effect as well.

The effects presented here can be extended to three-dimensional photonic crystals with little change. As a complete photonic band gap in three dimensions is not required, the crystal structure can be flexibly chosen. For experimental studies, an appropriate structure that quantitatively approximates our calculations could be a square lattice of air holes perforating a finite-height silicon slab, interacting with fast electrons, and operated near the communication wavelength. The same physics should apply to dielectric-in-air-type crystals as well. A practical issue is whether the radiation intensity is sufficiently strong to be observable for small  $v$ . Our numerical simulation indicates that, across a bandwidth of around 40%, the average radiation energy is roughly in a ratio of 1:1.5:4:20 for  $v/c = 0.1, 0.15, 0.3$ , and  $0.6$ . Furthermore, the radiation intensity at small  $v$  may even be much larger than these numbers in narrow bandwidths around specific frequencies, because of the unusual photon density of states in a photonic crystal. In conventional CR, for  $v > v_c$  an electron can emit hundreds of photons per centimeter of its path. Thus, for the velocities studied here, the emission rates correspond to a range starting from roughly 10 and ranging up to 200 photons per

centimeter, which should be amenable to direct experimental observation.

A number of applications also appear possible. Particles traveling at speeds below the phase-velocity threshold cannot be detected by conventional CR counters, and currently their observation relies on other devices, such as scintillation counters, proportional counters, or cloud chambers. These other devices, however, lack the unique advantages of strong velocity sensitivity and good radiation directionality as in conventional CR (2). With a photonic crystal, one should be able to achieve velocity selectivity and distinctive radiation patterns without any velocity threshold. Moreover, on the high-energy side, CR with a sharp radiation wavefront is possible for particles traveling through an all-air path inside a photonic crystal, allowing complete absence of the impurity scattering and random ionization losses inherent in a dense medium. This should improve the performance of present detectors. Finally, the CR frequency is set by the photonic crystal and is thus selectively scalable beyond optical wavelengths, opening up the possibility of flexible radiation sources for frequencies that are otherwise difficult to access.

### References and Notes

1. L. D. Landau, E. M. Lifshitz, L. P. Pitaevskii, *Electrodynamics of Continuous Media* (Pergamon, New York, ed. 2, 1984).
2. J. V. Jelly, *Cerenkov Radiation and Its Applications* (Pergamon, London, 1958).
3. I. M. Frank, *Nucl. Instrum. Methods Phys. Res. Sect. A* **248**, 7 (1986).
4. G. N. Afanasiev, V. G. Kartavenko, E. N. Magar, *Physica B* **269**, 95 (1999).
5. T. E. Stevens, J. K. Wahlstrand, J. Kuhl, R. Merlin, *Science* **291**, 627 (2001).
6. I. Carusotto, M. Artoni, G. C. L. Rocca, F. Bassani, *Phys. Rev. Lett.* **87**, 064801 (2001).
7. V. G. Veselago, *Sov. Phys. Usp.* **10**, 509 (1968).
8. J. B. Pendry, A. J. Holden, W. J. Stewart, I. Youngs, *Phys. Rev. Lett.* **76**, 4773 (1996).
9. J. B. Pendry, A. J. Holden, D. J. Robbins, W. J. Stewart, *IEEE Trans. Microwave Theory Tech.* **47**, 2075 (1999).
10. D. R. Smith, W. J. Padilla, D. C. Vier, S. C. Nemat-Nasser, S. Schultz, *Phys. Rev. Lett.* **84**, 4184 (2000).
11. R. A. Shelby, D. R. Smith, S. Schultz, *Science* **292**, 77 (2001).
12. R. A. Shelby, D. R. Smith, S. C. Nemat-Nasser, S. Schultz, *Appl. Phys. Lett.* **78**, 489 (2001).
13. S. J. Smith, E. M. Purcell, *Phys. Rev.* **92**, 1069 (1953).
14. K. F. Casey, C. Yeh, Z. A. Kaprielian, *Phys. Rev.* **140**, B768 (1965).
15. B. Lastdrager, A. Tip, J. Verhoeven, *Phys. Rev. E* **61**, 5767 (2000).
16. F. J. Garcia de Abajo, *Phys. Rev. Lett.* **82**, 2776 (1999).
17. K. Ohtaka, S. Yamaguchi, *Opt. Quantum Electron.* **34**, 235 (2002).
18. E. Yablonovitch, *Phys. Rev. Lett.* **58**, 2059 (1987).
19. S. John, *Phys. Rev. Lett.* **58**, 2486 (1987).
20. J. D. Joannopoulos, R. D. Meade, J. N. Winn, *Photonic Crystals: Molding the Flow of Light* (Princeton Univ. Press, Princeton, NJ, 1995).
21. M. Notomi, *Phys. Rev. B* **62**, 10696 (2000).
22. C. Luo, S. G. Johnson, J. D. Joannopoulos, J. B. Pendry, *Phys. Rev. B* **65**, 201104 (R) (2002).
23. C. Luo, S. G. Johnson, J. D. Joannopoulos, *Appl. Phys. Lett.* **81**, 2352 (2002).
24. The CR modes are excited with a strength proportional to the density of radiation states and  $\mathbf{q} \cdot \mathbf{e}^*_{\mathbf{k}'\mathbf{n}_G}$ , where  $\mathbf{k}'$  is the Bloch-reduced  $\mathbf{k}$  in the first Brillouin zone;  $\mathbf{G} = \mathbf{k} - \mathbf{k}'$ ; and  $\mathbf{e}^*_{\mathbf{k}'\mathbf{n}_G}$  is the  $\mathbf{G}$ -Fourier

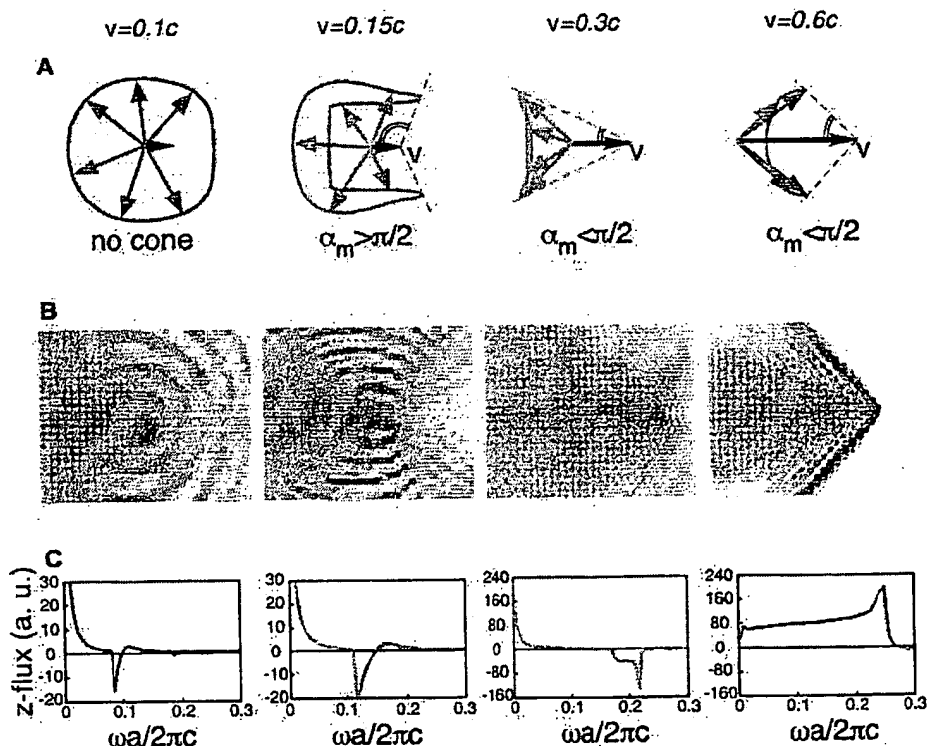


**Fig. 3.** FDTD simulation results for CR in the photonic crystal of Fig. 1. Each column represents the results for the value of  $v$  shown on the top. (A) Overall radiation cone shapes (dashed lines) deduced from the group velocity contours in Fig. 2C. (B) Distribution of the radiated magnetic field  $H_y$ . Blue, white, and red represent negative, zero, and positive field values, respectively. The color tables are chosen separately for best illustration in each case. (C) The frequency spectrum of the electromagnetic flux along  $z$  through a line perpendicular to  $v$ , in arbitrary units (a.u.).

- component of the Bloch electric field, as in  $E_{\text{ex}} = \sum_G e_{\text{kg}} e^{i(k+G) \cdot r}$ .
25. A. Yariv, P. Yeh, *Optical Waves in Crystals: Propagation and Control of Laser Radiation* (Wiley, New York, 1984), chap. 6.
26. The contour formed by  $u$  is similar to the ray surface in (29), though it now represents group velocities of different frequencies.
27. S. G. Johnson, J. D. Joannopoulos, *Opt. Express* **8**, 173 (2001).

28. The simulation uses a thick perfectly matched layer boundary region that overlaps 10 periods of the photonic crystal similar to that used in (30) and can absorb the Bloch waves away from a band edge. The moving charge is implemented as a point-like current density that is oriented toward the direction of motion and whose position depends on time.
29. M. Born, E. Wolf, *Principles of Optics: Electromagnetic Theory of Propagation, Interference and Diffraction of Light* (Cambridge Univ. Press, New York, ed. 7, 1999).

30. M. Koshiba, Y. Tsuji, S. Sasaki, *IEEE Microwave Wireless Components Lett.* **11**, 152 (2001).
31. Supported in part by NSF's Materials Research Science and Engineering Center program (grant no. DMR-9400334) and the Department of Defense, Office of Naval Research, Multidisciplinary University Research Initiative program (grant no. N00014-01-1-0803).

18 October 2002; accepted 5 December 2002

## A Reversibly Switching Surface

Joerg Lahann,<sup>1</sup> Samir Mitragotri,<sup>2</sup> Thanh-Nga Tran,<sup>1</sup>  
Hiroki Kaido,<sup>1</sup> Jagannathan Sundaram,<sup>2</sup> Insung S. Choi,<sup>1\*</sup>  
Saskia Hoffer,<sup>3</sup> Gabor A. Somorjai,<sup>3</sup> Robert Langer<sup>1†</sup>

We report the design of surfaces that exhibit dynamic changes in interfacial properties, such as wettability, in response to an electrical potential. The change in wetting behavior was caused by surface-confined, single-layered molecules undergoing conformational transitions between a hydrophilic and a moderately hydrophobic state. Reversible conformational transitions were confirmed at a molecular level with the use of sum-frequency generation spectroscopy and at a macroscopic level with the use of contact angle measurements. This type of surface design enables amplification of molecular-level conformational transitions to macroscopic changes in surface properties without altering the chemical identity of the surface. Such reversibly switching surfaces may open previously unknown opportunities in interfacial engineering.

Interfacial properties, such as wetting behavior, are defined by the molecular-level structure of the surface (1). Diverse modification procedures have been used to permanently alter wettability (2–4). Control of wettability has been recently demonstrated by elegant methods including light-induced (5–6) and electrochemical surface modifications (7–10). These systems require chemical reactions in order to control wettability.

We demonstrate an alternative approach for dynamically controlling interfacial properties that uses conformational transitions (switching) of surface-confined molecules. Polymers have been shown to undergo conformational reorientations when changed from one solvent to another (11) or from one temperature to another (12, 13) because of phase transitions between a well solvated and a poorly solvated state (14). In contrast, our approach maintains the system's environment unaltered (including solvent, electrolyte content, pH, temperature, and pressure) while

using an active stimulus, such as an electrical potential, to trigger specific conformational transitions (e.g., switching from an all-trans to a partially gauche oriented conformation; see Fig. 1). Amplification of conformational transitions to macroscopically measurable changes requires synergistic molecular reorientations of ordered molecules. In principle, this is attainable with a single-molecular layer, such as a self-assembled monolayer (SAM) of alkanethiolates on gold (15). However, the dense molecular packing in SAMs and the strong interactions between the methylene groups restrict dynamic molecular motions to the outermost atoms (16, 17). All in situ evidence so far indicates that applied electrical potentials have no effect on long-

chain alkanethiolate monolayers on gold within the range of chemical stability of the SAM (18). In other words, conventional SAMs are too dense to allow conformational transitions and consequently do not allow for switching. To explore SAMs as a model system for switching, we must establish sufficient spatial freedom for each molecule. Once a low-density SAM is created, preferential exposure of either hydrophilic or hydrophobic moieties of the SAM to the surrounding medium could be exploited for the switching of macroscopic surface properties.

(16-Mercapto)hexadecanoic acid (MHA) was chosen as a model molecule because it (i) self-assembles on Au(111) into a monolayer and (ii) has a hydrophobic chain capped by a hydrophilic carboxylate group, thus potentially facilitating changes in the overall surface properties. To create a monolayer with sufficient spacing between the individual MHA molecules, we used a strategy that exploits synthesis and self-assembly of a MHA derivative with a globular end group, which results in a SAM that is densely packed with respect to the space-filling end groups but shows low-density packing with respect to the hydrophobic chains. Subsequent cleavage of the space-filling end groups establishes a low-density SAM of MHA. The spatial dimensions of the precursor molecule to be used were adapted to match the optimum alkanethiolate density for conformational rearrangements.

The equilibrium low-energy conformational state of each of the sparsely packed MHA

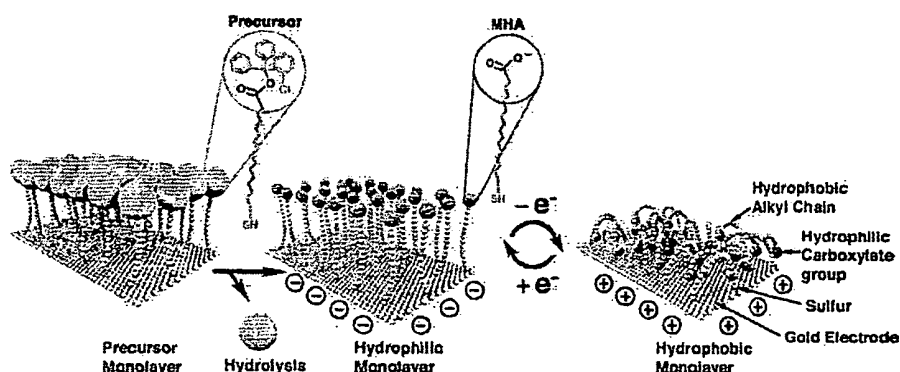


Fig. 1. Idealized representation of the transition between straight (hydrophilic) and bent (hydrophobic) molecular conformations (ions and solvent molecules are not shown). The precursor molecule MHA, characterized by a bulky end group and a thiol head group, was synthesized from MHA by introducing the (2-chlorophenyl)diphenylmethyl ester group.

<sup>1</sup>Department of Chemical Engineering, Massachusetts Institute of Technology (MIT), 45 Carleton Street, Cambridge, MA 02139, USA. <sup>2</sup>Department of Chemical Engineering, University of California at Santa Barbara, Santa Barbara, CA 93106, USA. <sup>3</sup>Department of Chemistry, University of California at Berkeley, Material Science Division, Lawrence Berkeley Laboratory, Berkeley, CA 94720, USA.

\*Present address: Department of Chemistry and School of Molecular Science (BK21), Korean Advanced Institute of Science and Technology, Daejeon 305-701, Korea.

†To whom correspondence should be addressed. E-mail: rlander@mit.edu